HAL
open science

Structural Inheritance Control on Intraplate Present-Day Deformation: GPS Strain Rate Variations in the Saint Lawrence Valley, Eastern Canada

Alizia Tarayoun, Stephane Mazzotti, Michael Craymer, Joseph Henton

To cite this version:

Alizia Tarayoun, Stephane Mazzotti, Michael Craymer, Joseph Henton. Structural Inheritance Control on Intraplate Present-Day Deformation: GPS Strain Rate Variations in the Saint Lawrence Valley, Eastern Canada. Journal of Geophysical Research, 2018, 123 (8), pp.7004-7020. 10.1029/2017JB015417 . hal-01934463

HAL Id: hal-01934463

https://hal.science/hal-01934463

Submitted on 26 Nov 2018

HAL is a multi-disciplinary open access archive for the deposit and dissemination of scientific research documents, whether they are published or not. The documents may come from teaching and research institutions in France or abroad, or from public or private research centers.

L'archive ouverte pluridisciplinaire **HAL**, est destinée au dépôt et à la diffusion de documents scientifiques de niveau recherche, publiés ou non, émanant des établissements d'enseignement et de recherche français ou étrangers, des laboratoires publics ou privés.

Journal of Geophysical Research: Solid Earth

RESEARCH ARTICLE
10.1029/2017JB015417

Key Points:
- Strong localization of intraplate deformation in areas of lithospheric-scale structural inheritance
- Quantification of the structural inheritance impact on surface deformation through comparison of GPS and GIA model strain rates
- Complex lateral strain rate variations within areas of structural inheritance

Supporting Information:
- Supporting Information S1

Correspondence to:
A. Tarayoun,
alizia.tarayoun@hotmail.fr

Citation:
Tarayoun, A., Mazzotti, S., Craymer, M., & Henton, J. (2018). Structural inheritance control on intraplate present-day deformation: GPS strain rate variations in the Saint Lawrence Valley, eastern Canada. *Journal of Geophysical Research: Solid Earth*, *123*, 7004–7020. https://doi.org/10.1029/2017JB015417

Received 3 JAN 2018
Accepted 19 JUL 2018
Accepted article online 27 JUL 2018
Published online 15 AUG 2018

©2018. American Geophysical Union. All Rights Reserved.

Structural Inheritance Control on Intraplate Present-Day Deformation: GPS Strain Rate Variations in the Saint Lawrence Valley, Eastern Canada

Alizia Tarayoun[1], Stéphane Mazzotti[1], Michael Craymer[2], and Joseph Henton[3]

[1]Géosciences Montpellier, Université de Montpellier, CNRS, Montpellier, France, [2]Geodetic Survey Division, Natural Resources Canada, Ottawa, Ontario, Canada, [3]Geodetic Survey Division, Natural Resources Canada, Sidney, British Columbia, Canada

Abstract Structural inheritance is one of the key factors commonly proposed to control the localization of strain and seismicity in continental intraplate regions, primarily on the basis of a first-order spatial correlation between seismicity and inherited tectonic structures. In this paper, we present new GPS (Global Positioning System) velocity and strain rate analyses that provide strong constraints on the magnitude and style of present-day strain localization associated with the inherited tectonic structures of the Saint Lawrence Valley, eastern Canada. We analyze 143 continuous and campaign GPS stations to calculate velocity and strain rate patterns, with specific emphases on the combination of continuous and campaign velocity uncertainties, and on the definition of robustness categories for the strain rate estimations. Within the structural inheritance area, strain rates are on average 2–11 times higher than surrounding regions and display strong lateral variations of the style of deformation. These GPS velocity and strain rate fields primarily reflect ongoing glacial isostatic adjustment (GIA). Their comparison with GIA model predictions allows us to quantify the impact of the structural inheritance and the associated lithosphere rheology weakening. Outside of the major tectonic inheritance area, GPS and GIA model strain rates agree to first order, both in style and magnitude. In contrast, the Saint Lawrence Valley displays strong strain amplification with GPS strain rates 6–28 times higher than model-predicted GIA strain rates. Our results provide the first quantitative constraints on the impact of lithospheric-scale structural inheritance on strain localization in intraplate domains.

1. Introduction

Intraplate seismicity can reach magnitudes up to 7–8, yet the dynamics of these earthquakes is a major current scientific question (e.g., Stein & Mazzotti, 2007). One of the difficulties in the study of intraplate deformation is that strain rates are low compared to those in plate-boundary regions. Typical expected strain rates for intraplate domains are ~10^{-13} to 10^{-10} year^{-1}, whereas plate boundary strain rates are ~10^{-8} year^{-1} or more (e.g., Calais et al., 2005; Gordon, 1998; Mazzotti & Adams, 2005; Sella et al., 2007).

A common hypothesis suggests that intraplate deformation is related to the reactivation of inherited structures (Adams & Basham, 1991; Coppersmith et al., 1987; Johnston, 1989). In other words, present-day deformation appears to concentrate primarily within areas of significant inheritance from past major tectonic events. Under this model, structural inheritance is considered on a lithospheric-scale, that is, domains of several tens to hundreds of kilometers affected by strong deformation of the whole crust and lithospheric mantle. Typically, those domains correspond to ancient plate boundaries of Paleozoic or older plate tectonic events. This definition excludes structures of local scales and thus limits the structural inheritance domains to large, plate-scale features. From seismic observations, Johnston (1989) showed that the largest worldwide intraplate earthquakes occurred along paleopassive margins or paleorifts located in continental interiors.

More recently, Mazzotti et al. (2005) quantified the surface deformation through Global Positioning System (GPS) measurements in a small part of the Saint Lawrence Valley (the Charlevoix area), eastern Canada (Figure 1), a domain with major faults inherited from Iapetus Ocean opening (~700 Myr) where GPS shortening rates are about twice higher than the regional average. The New Madrid seismic zone, eastern United States, is associated with a similar structural inheritance (Iapetus paleorift faults; Thomas, 2006), but the local deformation is highly debated. Frankel et al. (2012) suggest a significant motion across GPS sites of about 0.4 ± 0.1 mm/year, whereas Craig and Calais (2014) propose that the present-day deformation is below

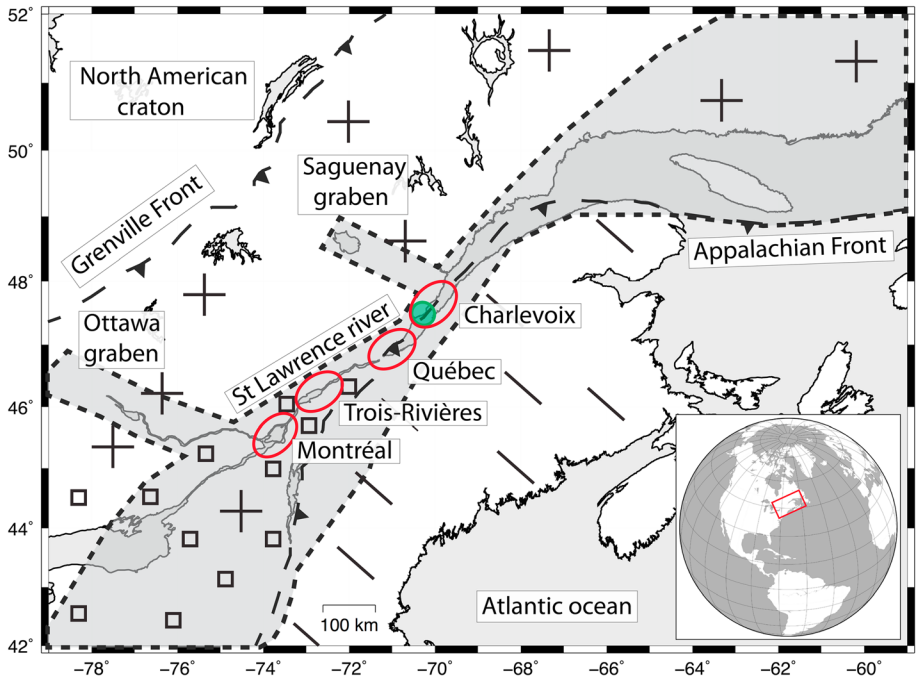

Figure 1. Tectonic setting of the Saint Lawrence Valley, eastern Canada. Dashed lines and gray region show the spatial extent of the Iapetan rifted margin (area of major structural inheritance). The Grenville, the Saint Lawrence Platform, and Appalachians geological provinces are displayed with cross, square, and line symbols, respectively. The main zones of interest are circled in red. The green area is the Charlevoix meteor impact location.

resolution of GPS data and that deformation may be variable in time. Thus, the presence of preferentially localized deformation within a structural inheritance area remains debated.

In this paper, we calculate the surface strain rates with new GPS data in the Saint Lawrence Valley and surroundings to investigate strain concentration within the structural inheritance area (Figure 1). The 143 continuous and campaign GPS stations with time series up to 17 years, a strong structural inheritance, and the presence of glacial isostatic adjustment (GIA) deformation (Mazzotti et al., 2005; Wu & Johnston, 2000; Wu & Mazzotti, 2007) should ensure measurable GPS signals. This makes the Saint Lawrence Valley a key area to provide answers on localization of deformation in structural inheritance domains, and to quantify the impact of structural inheritance on present-day surface deformation. The latter is quantified by comparing GPS strain rates, with special emphasis on robustness with modeled GIA strain rates. Differences between GPS and GIA signals are expected since GIA models are calculated with a uniform mantle rheology, while GPS signals include lateral rheological variations supposedly induced by structural inheritance.

The Saint Lawrence Valley displays strong lateral variations in earthquake patterns that raise the question of the role of structural inheritance in the localization of deformation and seismicity. This also raises the question of seismicity concentration as static (long-term) or transient (short-term) indicators of strain localization. Thus, investigating where surface deformation occurs has fundamental implications for understanding the processes driving intraplate deformation and intraplate earthquakes. These questions are currently debated. Our results provide the first quantitative estimation of the impact of structural inheritance and will provide additional input for this discussion.

2. The Saint Lawrence Valley

2.1. Tectonic and Geological Setting

The Saint Lawrence Valley has experienced two complete Wilson cycle since ~1.3 Gyr (Thomas, 2006), leading to strong structural inheritance (Figures 1 and 2). The Grenville orogeny took place from ~1.3 to 1 Gyr during the assembly of the Rodinia supercontinent, by accretion of allochtonous terranes to the SE margin of the Laurentia craton (North America; Hoffman, 1991; Karlstrom et al., 2001). The opening of

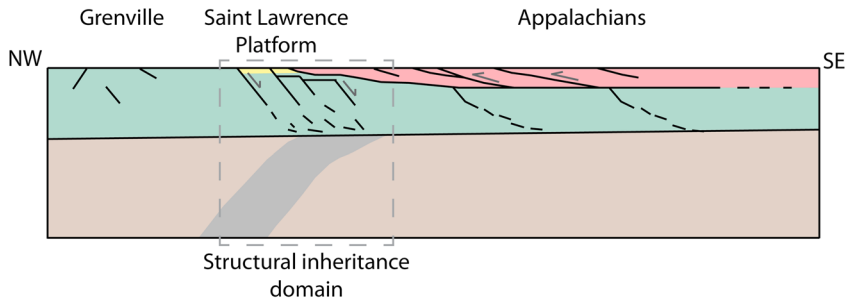

Figure 2. Schematic NW-SE cross section of the crust and upper lithospheric mantle. The green, yellow, and red areas represent the Grenville, Saint Lawrence Platform and Appalachians geological provinces. Brown domain represents the upper lithospheric mantle. The structural inheritance zone is defined as a domain with lithospheric-scale faults and shear zones.

the Iapetus Ocean ~700 Myr ago (Rankin, 1975) produced a rifted margin with a primary NE-SW orientation, as well as the orthogonal Ottawa and Saguenay grabens (Kumarapeli & Saull, 1966). The closing of the Iapetus Ocean occurred ~450 Myr ago during the Appalachian orogeny and resulting in thrusted units on the paleorift margin. The last major tectonic event in the Saint Lawrence Valley was the opening of the Atlantic Ocean ~150 Myr ago, leading to the reactivation of Iapetus normal faults (Lemieux et al., 2003; Tremblay et al., 2003). A meteorite impact with a crater of approximately 60 km diameter occurred ~350 Myr ago in southern Charlevoix creating a local normal fault system (Lemieux et al., 2003; Rondot, 1968). These faults, with an assumed depth of 10 km, are superimposed on Iapetus faults, creating a concentric area, which could further localize the deformation through fault intersections or reduced strength (Baird et al., 2009).

The last glaciation in the Saint Lawrence Valley was the Wisconsin glaciation extending from ~85 to 11 kyr, where the maximum ice extent spanned from 25 to 21 kyr. The final ice retreat in this region occurred at ~10–15 kyr (Dyke, 2004; Parent & Occhietti, 1988) inducing ongoing GIA in eastern Canada.

2.2. Structural Inheritance and Seismicity Setting

In this study, we define structural inheritance as paleoplate boundaries, that is, lithospheric-scale structures. In the Saint Lawrence Valley, such structures are related to the paleorift Iapetus and are localized between the Grenville and Appalachians provinces (Figure 2). In the crust, those structures comprise the paleomargin normal faults, mostly parallel to the Saint Lawrence River, such as the Saint Lawrence Fault that separates the Grenville province from the Saint Lawrence Platform (Lamontagne & Ranalli, 2014; Lemieux et al., 2003), the Charlevoix Fault located under the Saint Lawrence River, and the South Shore Fault under the Appalachians province imaged through gravity and magnetic data (Lamontagne et al., 2000). The Saint Lawrence area also displays second-order faults oriented approximately NW-SE and approximately E-W, corresponding to grabens and transfer faults, respectively (Tremblay et al., 2003). From seismic profiles, the major faults are imaged down to a maximum depth of ~30 km (Musacchio et al., 1997). Mechanical models show that rift structures are typically composed of shear zones in the lowermost crust and the lithospheric mantle (Gueydan et al., 2008), likely suggesting the presence of such kilometer-scale shear zones under the Saint Lawrence Valley. We consider this large fault system as the structural inheritance domain with a spatial scale of several tens or hundreds of kilometers (Figures 1 and 2), with a regional primary NE-SW orientation (Kumarapeli, 1985; Thomas, 2006).

The Saint Lawrence Valley displays strong spatial variations in seismic activity. Earthquakes are principally concentrated in the Lower Saint Lawrence Seismic Zone, Charlevoix Seismic Zone, and north of the Ottawa Graben (Figure 3). Between these areas, the seismicity is not clustered and sparse. The Charlevoix Seismic Zone has experienced the largest historical events in the Saint Lawrence Valley, with five earthquakes of magnitude approximately 6–7 in 1663, 1791, 1860, 1870, and 1925 (Adams & Basham, 1991). There are approximately 1,000 small earthquakes ($M \leq 4$) each year in the region. Earthquakes in the Saint Lawrence Valley reach a maximum depth of 30 km with, for the Charlevoix area, two thirds of the seismicity located between 7- and 15-km depth (Lamontagne et al., 2000).

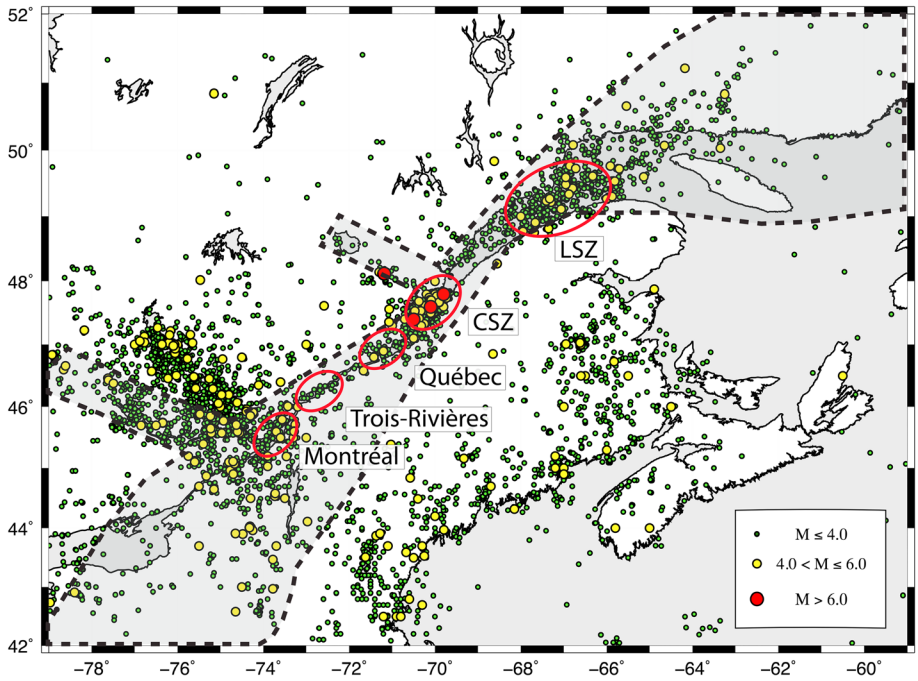

Figure 3. Historical and instrumental seismicity (1627 to 2016). The main zones of interest are circled in red. CSZ is for Charlevoix Seismic Zone, and LSZ is for Lower Saint Lawrence Seismic Zone. Dashed lines limit the structural inheritance domain.

3. GPS Data and Velocities

Because horizontal velocity and deformation signals in many intraplate regions are roughly at the level of GPS resolution, we pay specific attention to uncertainty sources and to the coherency of the GPS velocity field. In order to calculate strain rates using all available GPS stations, we implement a method to consistently combine continuous and campaign velocity uncertainties.

3.1. GPS Network and Data

We analyzed 143 GPS stations along the Saint Lawrence Valley from three continuous networks and two campaign networks: 11 stations from the national Canadian Active Control System, 22 continuous stations from the Québec provincial network, 11 continuous United States stations, 47 campaign stations of Canadian Baseline Network, and 52 campaign stations from a dense regional network dedicated to deformation study of the Saint Lawrence Valley. Continuous stations encompass the seismic region of the Saint Lawrence Valley and campaign stations are located in the near field (approximately 100 km) of the Iapetus inherited normal faults (Figure 4). The use of continuous and campaign data leads to four colocated stations and five almost colocated (less than 10 km apart) stations. Those colocated stations consist of a continuous and a campaign survey.

In our study, campaign data are acquired on three main types of monuments and foundations. The Canadian Baseline Network, dedicated to national and regional referencing, consists of concrete pillar monuments anchored either in bedrock or deep concrete foundations. Data are acquired over a minimum of 48-hr sessions every 2–4 years since the late 1990s. The stability and quality of this network are similar to that of geodetic continuous networks (Henton et al., 2006). In contrast, the specific dense Saint Lawrence network consists of tripod or steel mast monuments over geodetic markers. Thirty-six sites correspond to steel masts anchored to bedrock or massive erratic boulders, while the additional 16 sites are tripods or masts installed over benchmarks in soil cover. The Saint Lawrence campaign data comprise surveys of a minimum of 48 hr, repeated every 2 years at the same period (summer to early fall) and with similar types of antenna (e.g., Ashtech Choke-Ring) to optimize data stability. A summary of the episodic campaign survey and continuous data is provided in Tables S1 and S2 in the supporting information, respectively. Monuments of the Canadian Active Control System continuous network typically consist of concrete pillars anchored in bedrock. The longest time series range from 1999 to 2016. The average time series length is 13 years. Sites of the Québec

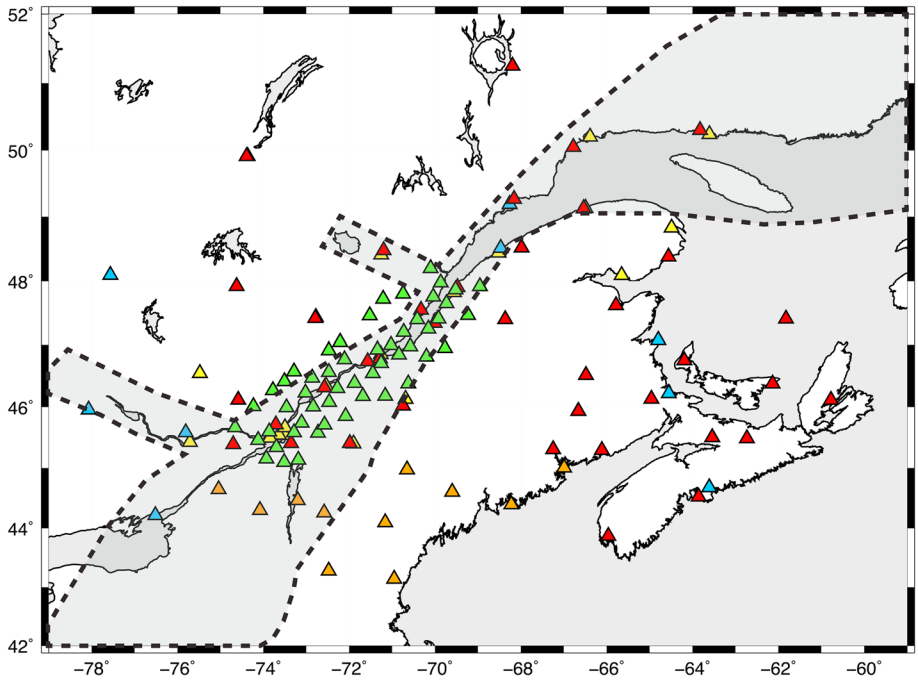

Figure 4. Global Positioning System stations. Green and red triangles are the Saint Lawrence and Canadian Baseline Network campaign networks, respectively. Blue, yellow, and orange triangles are Canadian Active Control System, Québec, and United States continuous networks, respectively. Dashed lines limit the structural inheritance domain.

provincial network are situated on building rooftops. All monuments are steel masts. The average time series length is 10 years. The United States stations are mostly masts on rooftops with an average time series length of 9 years.

Previous studies have shown that type of monument is not a dominant source of uncertainty in estimations of GPS velocities (e.g., Hackl et al., 2011; Langbein, 2008; Malservisi et al., 2013). Thus, we do not consider the monument type in uncertainty analysis of strain rates, other than through the velocities standard errors that reflect the site stability.

3.2. GPS Data Processing

GPS data are processed with the Natural Resources Canada Precise Point Positioning (PPP) software (Héroux & Kouba, 2001). Precise satellite orbits and clocks, and Earth rotation parameters used to calculate daily positions are from the International Global Navigation Satellite System Service precise products (Dow et al., 2009). The ocean tide loading is corrected using the FES2004 model (Lyard et al., 2006). Tropospheric delays are modeled using the meteorological model Vienna Mapping Functions 1 (Boehm et al., 2006). Velocities are expressed relative to the stable North American plate, defined in the ITRF2008 reference frame (Altamimi et al., 2012). Nguyen et al. (2016) tested several options of the PPP processing in order to estimate the quality of daily positions and deduced velocities. They found that impact of the parameterization choices is mainly dependent to the duration of the time series and could impact velocities up to 0.5 mm/year (mean difference of GPS velocities between several processing options). In order to ensure an optimal solution, we based our data processing on their study.

Because position and velocity precision is a critical issue for intraplate deformation studies, we tested the repeatability of the calculated positions and velocities by comparing our reference PPP solution with a double-difference solution using GAMIT 10.6 (Herring et al., 2015). Mean velocity differences between the PPP and GAMIT solutions for 55 campaign stations of the Saint Lawrence network are 0.04, −0.10 and 0.35 mm/year with a standard error of 0.05, 0.03 and 0.15 mm/year for the north, east, and vertical components, respectively (Figure S1). The differences in the network mean velocities are due to differences in the reference frame realization between the two solutions and do not affect strain rate computations. The dispersions in the PPP and GAMIT solutions are similar at about 0.1 mm/year. This illustrates the quality of both

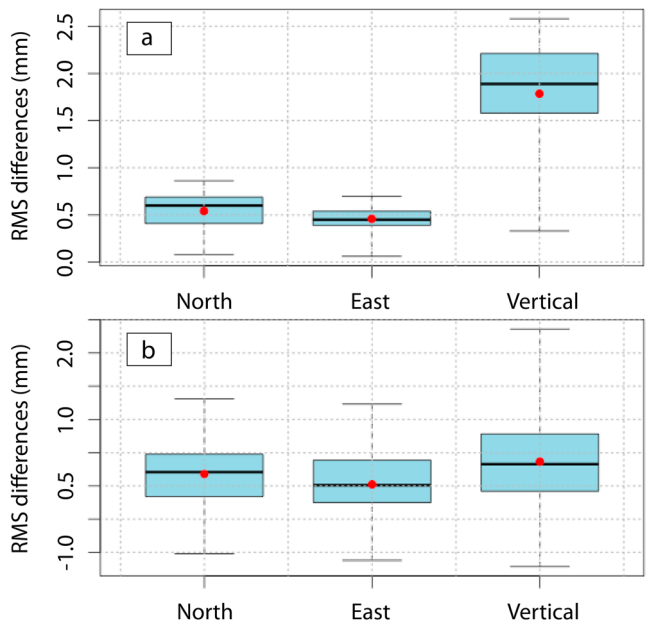

Figure 5. Influence of common-mode correction on daily positions. Whisker plots of the position dispersions (root-mean-square, RMS) differences between the original and the common-mode postcorrection for continuous (a) and campaign (b) data. A positive RMS difference implies a reduction in dispersion after the common-mode correction. The whisker diagrams show the quartiles and extremes. Red points are the mean.

solutions, owing to the precise International Global Navigation Satellite System Service products, and provides a first-order estimation of the velocity resolution for our data set.

Daily GPS positions can be influenced by signals that are spatially coherent at the scale of the regional network and are not related to tectonic processes (e.g., satellite ephemerides and regional hydrology; Wdowinski et al., 1997). In order to better define the long-term velocities, we correct our GPS position time series for an empirical common-mode signal assumed to affect all networks. This common mode is calculated by stacking the residual time series, after removing a linear trend, of the 37 continuous stations that cover the whole study area and have the longest time period. The stack starts in 2001.000 and stops in 2016.765, thus restraining the maximal length of time series for all stations (Figure S2). Figure 5 shows the differences of root-mean-square (RMS) values of daily positions with and without the common-mode correction. A reduction of RMS for all continuous stations is observed, leading to lower position dispersion, which is commonly found (Wdowinski et al., 1997; Williams et al., 2004; Zhu et al., 2017). In contrast, we observe a much smaller effect of the common-mode correction on campaign stations. Roughly half of the stations show reduced RMS up to 2.4 mm, whereas half show increased RMS up to 1.2 mm. Despite its negligible effect, we apply the common-mode correction to campaign stations to ensure homogeneous processing for continuous and campaign data. Means RMS after correction are 1.7, 2.5, and 4.4 mm for continuous stations and 2.7, 3.5, and 5.6 mm for campaign stations for the north, east, and vertical components, respectively.

3.3. GPS Velocity Uncertainties

In order to calculate formal uncertainties on GPS velocities, we use the formulation of Williams (2003) for continuous stations, which provides velocity standard errors on the basis of the noise characteristics (amplitude and spectral index) of the position time series. We find average spectral indices of −0.8, −0.7, and −0.6 for the north, east, and vertical components, respectively, similar to recent studies (either PPP or double-difference processing; e.g., Hackl et al., 2011; Nguyen et al., 2016; Njoroge et al., 2015; Santamaría-Gómez et al., 2011). These indices are symptomatic of flicker noise (spectral index of −1) with a small component of white noise (index of 0), suggesting a relatively fast convergence of the velocities for long time series (ca. 10 years).

The calculation of strain rates uses both continuous and campaign data and thus requires that the velocity standard errors be coherent for the two data sets. Due to their very low sampling, campaign data do not provide information on the noise characteristics. Thus, we assume that noise processes affecting campaign stations are similar to those of continuous stations, and we apply a simplified analytical expression for flicker noise uncertainty σ_F (Mao et al., 1999):

$$\sigma_F = \left(\frac{\alpha \times \mathrm{RMS}^2 \times 1.78}{g^{0.22} \times T^2}\right) \tag{1}$$

where g is the percentage of daily positions per year, T is the length of the time series (year), and RMS (mm) is the mean dispersion of daily positions of continuous stations, used as a proxy for the noise amplitude by applying a scale factor α (mm^{-1}·year) calibrated using the 37 longest continuous time series (cf. Marechal et al., 2015).

This analytical expression (equation (1)) allows calibrating the velocity standard errors for campaign data using the noise characteristics of continuous data. The scale factor (14.7, 4.8, and 3.3 mm^{-1}·year for the north, east, and vertical components, respectively) is calculated by equating the velocity standard errors of continuous stations derived using the Williams (2003) formulation to those derived using equation (1). The differences in standard error estimations between the two formulations are on average 0.03, 0.05, and 0.06 mm/year for the north, east, and vertical components, respectively, indicating that the simplified expression (equation (1)) yields reasonable uncertainties at the 0.1 mm/year level.

Table 1
Mean Velocity Standard Errors

	North		East		Vertical	
	σW	σF	σW	σF	σW	σF
Permanent sites	0.01	0.21	0.02	0.15	0.03	0.23
Campaign sites	0.18	0.91	0.24	0.77	0.38	1.12

Note. Based on white (σ_W) and colored (σ_f) noise models (mm/year).

Mean velocity standard errors for the whole network are given in Table 1. The mean standard errors on campaign data (approximately 1 mm/year) are significantly larger than the velocity variability due to data processing (approximately 0.1 mm/year; cf. section 3.2). This difference suggests that our formal velocity standard errors may be conservative, which will impact our strain rate analysis (cf. section 4.1). Hereafter, GPS velocities are quoted with their formal standard error ($v \pm \sigma$) based on the colored noise (flicker noise) analysis.

A comparison is made with the white noise approach, which is commonly used in campaign GPS study and underestimates the standard errors by a factor of 3–5 (Mao et al., 1999). Standard errors for campaign stations are higher than those for continuous stations by a factor of 2–3 depending primarily on the length of time series. With a 10-year-long record, the difference of standard error is about 0.6 mm/year between continuous and campaign stations in the horizontal component (Figure S3).

3.4. GPS Velocities

The complete campaign and continuous residual velocity field is shown in Figure 6 and listed in Table S3. At first order, the continuous and campaign velocities show a good coherence (both magnitudes and orientations). Among the nine colocated or nearly colocated stations, only one case presents a continuous and a campaign velocity pointing in opposite directions, although the two are compatible within their standard errors. We observe a strong NW-SE regional gradient of the horizontal velocities decreasing from 1.9 to 0.1 mm/year with a mean velocity of 0.6 mm/year. This horizontal gradient is locally affected by small-scale perturbations. Vertical velocities display a similar regional gradient, from 10.4 to −2.9 mm/year, that is mostly linear except in the Saint Lawrence Valley where there are strong local variations. This velocity field is consistent with Mazzotti et al. (2005) and Lamothe et al. (2010), which focused on the Charlevoix area, and with Goudarzi et al. (2016) focused on eastern Canada. This NW-SE velocity gradient is compatible with the GIA process due to a maximal ice thickness centered in the Hudson Bay (Goudarzi et al., 2016; Tushingham & Peltier, 1991). The local variations in the velocity field relative to the long-wavelength GIA signal may be indicative of local strain concentrations and are addressed in the following section using strain rate analysis.

4. Strain Rates

4.1. Strain Rate Calculations and Robustness Evaluation

Numerous methods exist to derive strain rates from GPS velocities (Goudarzi et al., 2015), commonly using gridded or interpolation techniques (e.g., El-Fiky et al., 1997; Hackl et al., 2009). In order to study strain rates over a variety of regions and scales and over specific zones, we use a simple uniform-domain approach, in which we calculate strain rate tensors in a given region assuming that the GPS velocities can be decomposed into a combination of translation, strain, and rigid rotation rates, including the volumetric strain rate due to vertical motion (Malvern, 1969; Mazzotti et al., 2005). The primary assumption is that the deformation is uniform over the analyzed region, with the six deformation parameters (and their uncertainties) indicative of the average tectonics over region spatial scale. This method, compared to a more common gridded technique, allows us to better estimate the robustness of the strain rates and their variations over a variety of regions and spatial scales that would otherwise be smoothed and interpolated.

The horizontal strain rate tensors are expressed as following:

$$\begin{aligned} \dot{\varepsilon}_{XX} &= \frac{\partial V_X}{\partial X} + \frac{V_Z}{R} \\ \dot{\varepsilon}_{YY} &= \frac{\partial V_Y}{\partial Y} + \frac{V_Z}{R} \\ \dot{\varepsilon}_{XY} &= \frac{1}{2}\left(\frac{\partial V_X}{\partial Y} + \frac{\partial V_Y}{\partial X}\right) \end{aligned} \tag{2}$$

where (X,Y,Z) are the local north, east, and vertical axes of a Cartesian reference system centered on the barycenter of the GPS stations and R is the radius of the Earth. Vertical velocities are taken into account in the

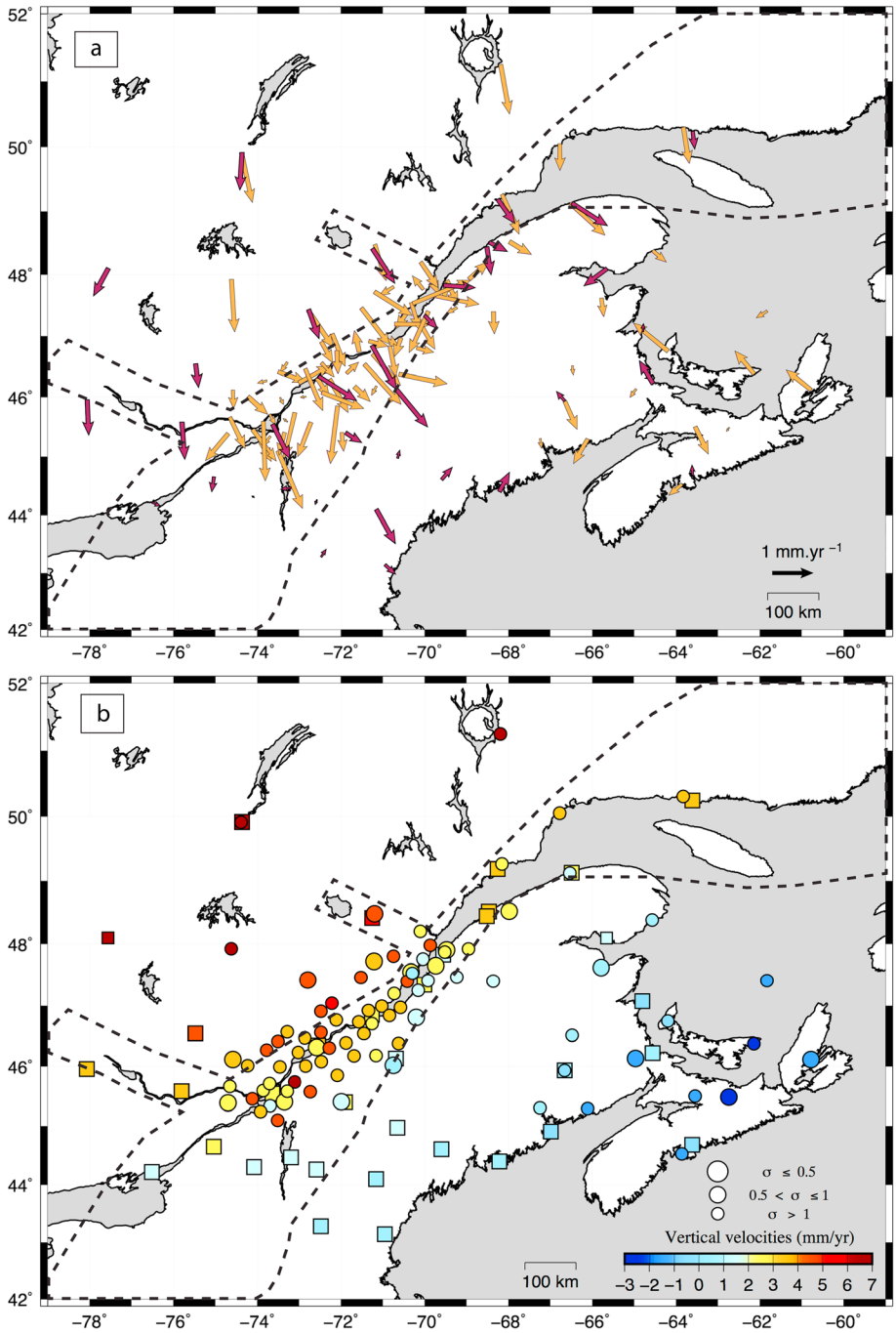

Figure 6. Global Positioning System velocity field with respect to stable North America. (a) Horizontal velocity field. Red and orange vectors are velocities for continuous and campaign stations, respectively (for better visibility, standard errors are not represented, cf. Table S3). (b) Vertical velocity field. Velocities are displayed in the color scale, and symbol sizes indicate the standard error range. Squares and circles are continuous and campaign stations, respectively. Dashed lines limit the structural inheritance domain.

calculation of the horizontal strain rate tensors since their magnitudes are commonly larger than horizontal velocities in GIA controlled domains. The magnitude of translation, strain, and rotation rates are calculated using a standard least squares inversion. This allows calculating standard errors on all parameters that take into account both the quality of the fit and the velocity standard errors. The calculated strain rates are expressed in terms of magnitudes and azimuths of the two principal components of the tensors (*e*1 and *e*2).

Table 2
Strain Rates and Standard Errors for Each Zone (Figure 8)

Zones	*e*1	σ_f *e*1	*e*2	σ_f *e*2	*az*	σ *az*	σ_n	σ_b *e*1	σ_b *e*2	*OVL e*1	*OVL e*2
1	3.42E−9	1.04E−9	1.39E−9	2.24E−9	87.98	31.61	1.59E−9	5.12E−10	6.71E−10	0.057	0.32
3	1.54E−9	8.27E−10	−6.09E−9	2.56E−9	30.25	10.55	1.72E−9	7.64E−10	2.17E−9	0.26	0.11
4	3.90E−10	4.18E−10	−3.21E−9	7.93E−10	55.73	5.51	5.28E−10	2.06E−10	1.88E−10	0.28	1.40E−15
5	1.57E−9	5.94E−10	−2.75E−9	6.83E−10	82.37	8.75	6.50E−10	1.38E−10	4.21E−10	0.041	0.024
6	−3.70E−11	4.74E−10	−4.92E−9	8.66E−10	77.17	5.38	6.38E−10	2.92E−10	2.51E−10	0.6	2.60E−7
7	2.79E−9	3.72E−10	−4.61E−10	3.23E−10	96.81	5.39	3.38E−10	6.92E−10	4.21E−10	0.005	0.46
8	1.18E−9	8.22E−10	2.76E−10	3.57E−10	40.28	27.12	5.84E−10	3.10E−10	3.86E−10	0.061	0.38
9	1.92E−9	1.15E−9	−1.46E−9	1.81E−9	145.94	18.9	1.39E−9	7.95E−10	1.33E−10	0.25	0.12
10	4.13E−9	2.76E−9	−3.59E−9	2.53E−9	82.26	14.94	2.51E−9	6.83E−10	2.38E−9	0.08	0.18
11	−1.54E−9	1.67E−9	−6.81E−9	4.68E−9	44.59	25.03	3.08E−9	1.36E−9	1.03E−9	0.34	0.054
14	3.88E−9	4.05E−9	2.70E−9	2.54E−9	167.2	104.21	3.02E−9	4.50E−10	6.30E−10	0.11	0.27
15	5.22E−9	1.73E−9	−7.35E−10	1.03E−9	88.35	9.8	1.29E−9	5.32E−10	1.93E−9	0.005	0.2
16	3.44E−9	8.47E−10	−4.73E−9	1.10E−9	105.28	3.8	8.16E−10	2.00E−9	1.22E−9	0.024	1.10E−12
18	9.41E−9	8.87E−9	−3.86E−9	8.29E−9	163.38	27.34	8.02E−9	8.73E−9	9.54E−10	0.11	0.14
21	1.05E−8	8.25E−9	−2.27E−11	8.75E−9	77.75	31.64	7.50E−9	2.47E−9	2.56E−9	0.2	0.38
22	5.48E−9	3.12E−9	−1.71E−8	1.69E−8	31.35	23.38	1.14E−8	2.22E−9	1.11E−9	0.24	0.062
23	7.56E−9	8.97E−9	−1.83E−8	1.44E−8	69.94	18.13	1.13E−8	1.21E−9	3.83E−9	0.12	0.1
24	1.24E−8	2.01E−8	−4.57E−9	1.55E−8	4.37	41.25	1.62E−8	6.46E−9	4.75E−9	0.38	0.37
25	1.12E−9	8.34E−9	−8.06E−9	1.40E−8	68.37	47.93	1.06E−8	1.99E−9	2.95E−9	0.33	0.21
26	1.40E−8	8.51E−9	−7.55E−9	8.92E−9	128.6	16.55	8.07E−9	4.15E−9	1.66E−9	0.14	0.19
28	2.00E−8	1.98E−8	−1.80E−9	1.35E−8	0.81	30.4	1.53E−8	7.87E−9	7.13E−9	0.22	0.4
29	1.00E−8	9.92E−9	−2.07E−9	8.36E−9	173.4	30.81	8.42E−9	1.87E−9	1.04E−9	0.13	0.19
30	−2.16E−9	1.23E−8	−2.04E−8	1.26E−8	26.06	32.63	1.20E−8	2.16E−9	5.80E−9	0.32	0.21
31	1.99E−8	2.65E−8	−6.28E−9	9.30E−9	149.91	28.53	1.86E−8	1.16E−8	7.55E−10	0.37	0.093

Note. *e*1 and *e*2: principal components of the strain rate tensor, and σf: their standard errors (year^{-1}); *az*: azimuth relative to north of *e*1 and σ *az*: its standard error (°); σ_n: standard error of the mean noise level (year^{-1}); σ_b *e*1 and σ_b *e*2: standard errors of strain rate from the bootstrap analysis (year^{-1}); *OVL e*1 and *OVL e*2: overlap coefficients of *e*1 and *e*2.

Because of the low signal-to-noise ratio of both horizontal velocity and strain rate data, we carry out a detailed analysis of the strain rate uncertainties that do not only rely on the standard errors from the least square inversion but also include statistical analysis based on the GPS velocity standard errors and spatial distribution. Details of the method and results are provided Figures S5–S37 in the supporting information. For each region, the analysis consists in three steps:

1. Estimation of the region average strain rate noise level, using a Monte Carlo simulation based on the GPS velocity standard errors (with a null velocity field, i.e., zero-strain-rate hypothesis).
2. Estimation of the actual strain rate distribution, using a bootstrap simulation based on the GPS velocities, in order to account for their number, variability, and geographical distribution.
3. Estimation of the Overlap Coefficient (OVL) between the noise level (1) and actual strain rate (2) distributions as a measure of the significance (difference from the noise) of the actual strain rate.

For each region, the robustness of strain rate principal components can be assessed using: their formal standard errors (σ_F) derived from the least squares inversion (equation (2)), the standard error of the average noise level (σ_N), the standard error of the bootstrap distribution (σ_B), and the Overlap Coefficient (OVL). These values are given in Table 2, and three examples are shown in Figure 7. In all cases, the formal and noise standard errors are similar and systematically larger than the bootstrap standard errors (on average 2.2 times):

$$\sigma_F \approx \sigma_N > 2.2\ \sigma_B \tag{3}$$

Thus, formal strain rate standard errors are primarily due to the GPS velocity standard errors, whereas the variability and spatial distribution of the velocities have a smaller contribution (on average 50% smaller). This observation suggests that the GPS velocity standard errors are slightly overestimated compared to the regional coherence of the velocity field, in particular for campaign velocities that

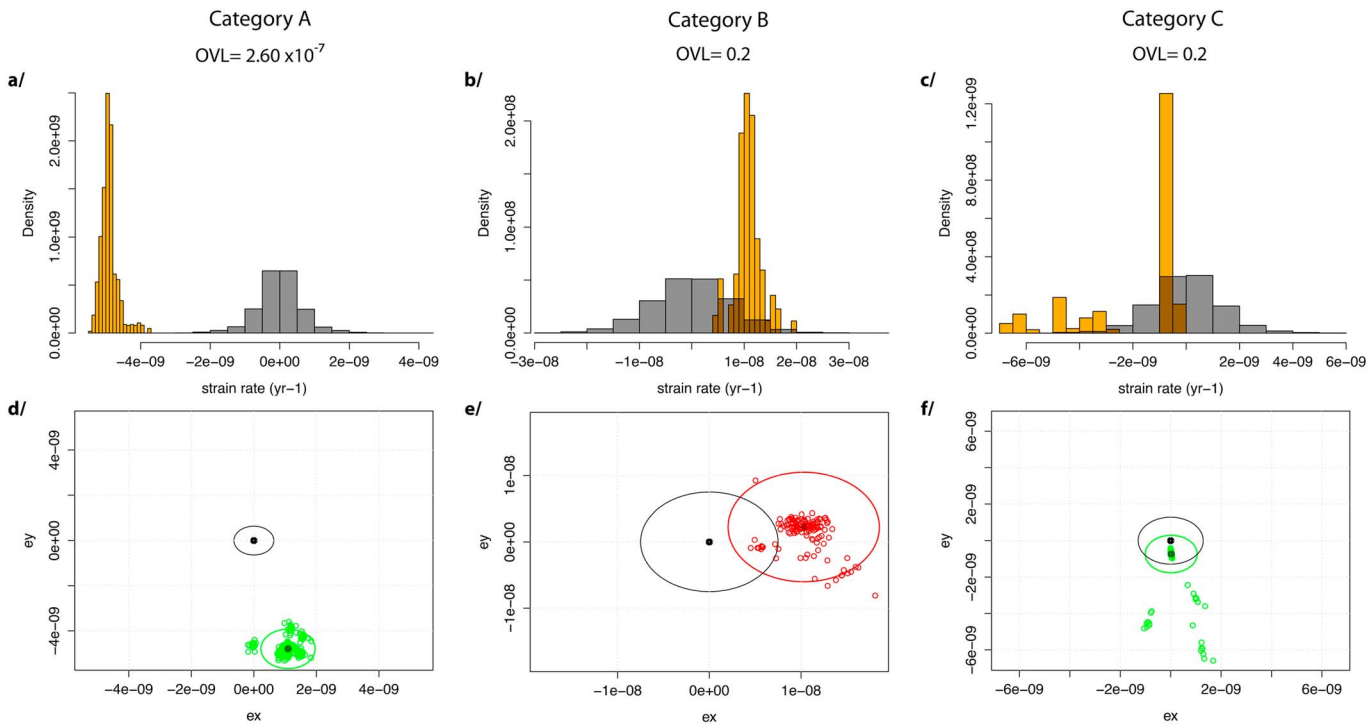

Figure 7. Examples of strain rate uncertainty and robustness analysis. Categories A–C correspond to zone numbers 6, 21, and 15, respectively (Figure 8). OVL is the overlap coefficient (range between 0 and 1, cf. text). (a)–(c) show strain rate of mean noise from Monte Carlo method (gray) and strain rate from bootstrap method (orange) histograms for the largest principal strain rate tensor components. (d)–(f) show a 2-D view of the principal component distribution based on the bootstrap simulation (red and green points represent *e*1 and *e*2, respectively). Dark red/green points and the associated ellipses represents the mean and standard error of the principal component from the least squares inversion. Gray points and the associated ellipses are the mean and standard error of the noise based on the Monte Carlo simulation.

constitute the bulk of our data set. Thus, in order to discuss the significance of the strain rate estimations, we choose to rely on a statistical analysis that combines the noise level and the bootstrap distributions, rather than simply relying on the formal standard errors.

The OVL coefficient is a measure of the similarity between two sets, in our case of the area of intersection between the bootstrap and noise distributions. Thus, it provides a measure of the significance of the measured strain rate (in terms of difference from the noise), with values ranging from 0 (no overlap, very high significance) to 1 (full overlap, no significance); compare Figure 7. In practice, OVL values of 0.04 and 0.29 can be used to represent 95% and 68% confidence levels, that is, cases in which the bootstrap and noise distributions differ at two and one standard errors, respectively (cf. additional information of the strain rate robustness assessment in the supporting information). Based on these OVL thresholds, we define three robustness categories for our strain rate estimations:

1. Strain rates with $OVL \leq 0.04$, that is, a 95% confidence level (Figure 7a). Strain rates in this category are all significant at 95% relative to their formal standard errors (σ_F), except that of zone 11.
2. Strain rates with $0.04 < OVL \leq 0.29$, that is, a 68% confidence level (Figure 7b). They often present a confidence level of 68% relative to their formal standard errors (σ_F).
3. Strain rates for which we can define the style but not the magnitude. This category comprises cases with $OVL \leq 0.29$ but that display very large bootstrap dispersions, as well as cases with $OVL > 0.29$ but that display systematically negative or positive bootstrap distributions indicating a consistent style of deformation (Figure 7c).

Hereafter, we only present and discuss the results in those three categories, leaving aside results with low confidence levels (results for all strain rates are provided Table S4 in the supporting information). All strain rate values are given with their formal standard error ($e_{1,2} \pm \sigma_{F1,2}$) and the associated OVL coefficient or robustness category (cat.).

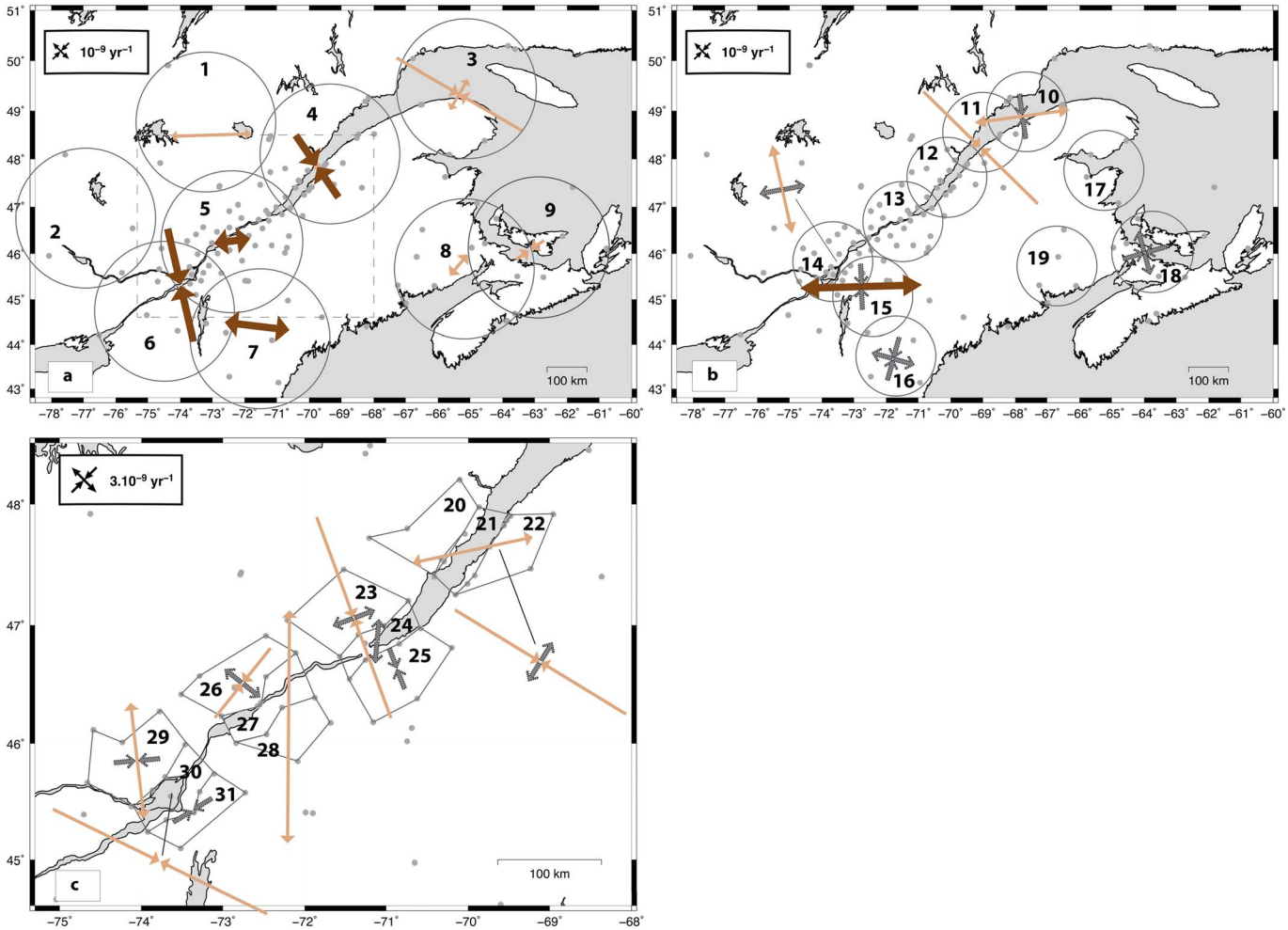

Figure 8. Global Positioning System horizontal strain rates. Dark brown, light brown, and gray arrows show the strain rate principal components for each analyzed regions for robustness categories A–C. Empty regions are those with results that are not significant (Table S4). Gray points represent the Global Positioning System stations. (a)–(c) show strain rates on large (350 km), medium (200 km), and small (50–100 km) spatial scales, the latter focused on the Saint Lawrence Valley. The dashed rectangle in (a) shows delimitation of the map in (c).

4.2. Strain Rate Results

Figure 8a presents the strain rate results for large spatial scales (350-km diameter). The circular regions are chosen to represent the three geological provinces (Grenville, Saint Lawrence Platform, and Appalachians, cf. Figure 1), with the maximum number of GPS sites within the area. The strain rate patterns can be divided into three main domains:

1. In the Grenville province, we observe a significant extension of $(3.4 \pm 1.0) \times 10^{-9}$ year^{-1} oriented roughly E-W (cat. B). The mean vertical velocity for this region is 6.8 ± 0.8 mm/year, contributing about 1.4×10^{-9} year^{-1} of isotropic extension, about half of the surface strain rate.
2. Among the four zones along the Saint Lawrence Valley, three display a NW-SE to NNW-SSE shortening with magnitude up to $(6.1 \pm 2.6) \times 10^{-9}$ year^{-1} (in Zone 3, cat. B). In contrast, Zone 5 displays a well-defined E-W extension ($[1.6 \pm 0.6] \times 10^{-9}$ year^{-1}, cat. A). The deformation style in Zones 3, 4, and 6 corresponds to that inferred from earthquake focal mechanisms that are mainly associated with NW-SE shortening, although significant variations are observed in the Charlevoix region (Mazzotti et al., 2005; Mazzotti & Townend, 2010).
3. In the Appalachians province, strain rates are lower than those of Grenville and the Saint Lawrence Platform provinces and display opposite deformation style in the Maritime Provinces (Zones 8 and 9). Earthquake focal mechanisms and stress data in the Maritime Appalachians indicate mainly an ENE-

WSW shortening (Mazzotti & Townend, 2010), compatible with the strain rate observed in Zone 9 but opposite to that of Zone 8. Zone 7, which is included in the Saint Lawrence Platform and Appalachians provinces display an E-W extension.

Reducing the size of the analyzed regions indicates a more complex pattern of deformation along the Saint Lawrence River, that is, in the region of major structural inheritance. Figure 8b presents strain rates calculated in circular regions of 200 km of diameter. Half of the regions are not in categories A, B, or C and cannot be exploited. The remaining regions are compatible with the large-scale observations (e.g., Zones 11 vs. 4 and 18 vs. 9), except for the southern Saint Lawrence area where the intermediate-scale strain rates are in sharp contrast with the large-scale ones (Zones 14 vs. 6). These variations may indicate short-wavelength perturbations in the strain rate patterns, but because of the rather low robustness of these results, we focus on a smaller scale to investigate these potential variations.

Figure 8c presents strain rates on a spatial scale of 50–100 km, centered on the Saint Lawrence Valley. The regions are chosen to follow the four primary seismic zones: Charlevoix, Québec, Trois-Rivières, and Montréal (cf. section 2.2 and Figure 3). Because the seismicity mostly concentrates beneath the Saint Lawrence River, we calculate in every four cases strain rates in domains north, along, and south of the river. It is important to note that, despite the small spatial scale and relatively small number of stations in each zone, one third of the calculated principal components fall in the robustness category B (68% confidence level according to the OVL analysis), while another third are in category C (information on style but not magnitude).

At this scale, the deformation styles display very strong lateral variations. The most surprising observation is in the Charlevoix region, where the central zone (21) presents a roughly E-W extension rate of $(10.5 \pm 8.2) \times 10^{-9}$ year^{-1} (cat. B), in strong contrast with the NW-SE shortening rate observed on the south shore (Zone 22) and on a larger scale (Zone 4; Mazzotti et al., 2005). Although the extension style in the central zone only falls in category B, the result appears significantly different from the background noise level (cf. Figures S5–S37 in the supporting information). This contrast between the central zone (extension) and the north and south shores (shortening) is also observed in the Quebec City area (Zones 23–25), albeit with a lower level of robustness as only the style of deformation can be defined. This pattern of deformation reverses in the southwestern part of the Saint Lawrence Valley (Montréal area), where the central domain (Zone 30) is associated with strong NW-SE shortening ($[20.4 \pm 12.6] \times 10^{-9}$ year^{-1}, cat. B), whereas the north shore shows N-S extension (Zone 29, $[10.0 \pm 9.9] \times 10^{-9}$ year^{-1}, cat. B).

At this scale, GPS strain rates within the structural inheritance area are on average 4–11 times higher than in the Grenville ($3.4 \pm 1.0 \times 10^{-9}$ year^{-1}) and Appalachians ($1.2 \pm 0.8 \times 10^{-9}$ and $1.5 \pm 1.8 \times 10^{-9}$ year^{-1}) provinces (outside the structural inheritance area).

4.3. Comparison Between GPS and GIA Model Strain Rates

The main process at the origin of present-day deformation in the Saint Lawrence Valley region is GIA (e.g., Mazzotti et al., 2005; Wu & Johnston, 2000). To quantify the influence of structural inheritance on the localization of GIA-driven deformation, we compare the observed GPS strain rates with model-predicted GIA strain rates. The latter are calculated from velocity predictions at the GPS sites based on the ICE6G_C (VM5a) model (Peltier et al., 2015). ICE6G GIA model is the most up-to-date realization of global models and includes, among others, vertical geodetic data worldwide. It assumes a laterally uniform viscosity structure of the Earth; thus, rheology variations associated with structural inheritance in the Saint Lawrence Valley can be expected to result in significant differences between the observed strain rates and the GIA model predictions.

Figure 9 presents the comparison between GPS and GIA model strain rates for each region defined in Figures 8a and 8c. To first order, GPS and GIA strain rates are similar at large spatial scale (Figure 9a), including the spatial variations of strain rate style along the Saint Lawrence River (cf. NW-SE shortening in Zone 4 vs. E-W in Zone 5). Similarly, a central N-S band of E-W extension that crosses the Grenville, Saint Lawrence Platform, and Appalachians provinces (Zones 1, 5, and 7) is observed in the GPS data and GIA model, at the transition between two domains of NW-SE outward motion and shortening (Mazzotti, 2007). At this scale, GPS strain rates are 1–3 times larger than the GIA strain rates. This result confirms the primary role of GIA as a driver of long-wavelength (hundreds of kilometers) deformation and illustrates the quality of the GPS-derived strain rates that are precise enough to extract strain patterns at the $(2–3) \times 10^{-9}$ year^{-1} level.

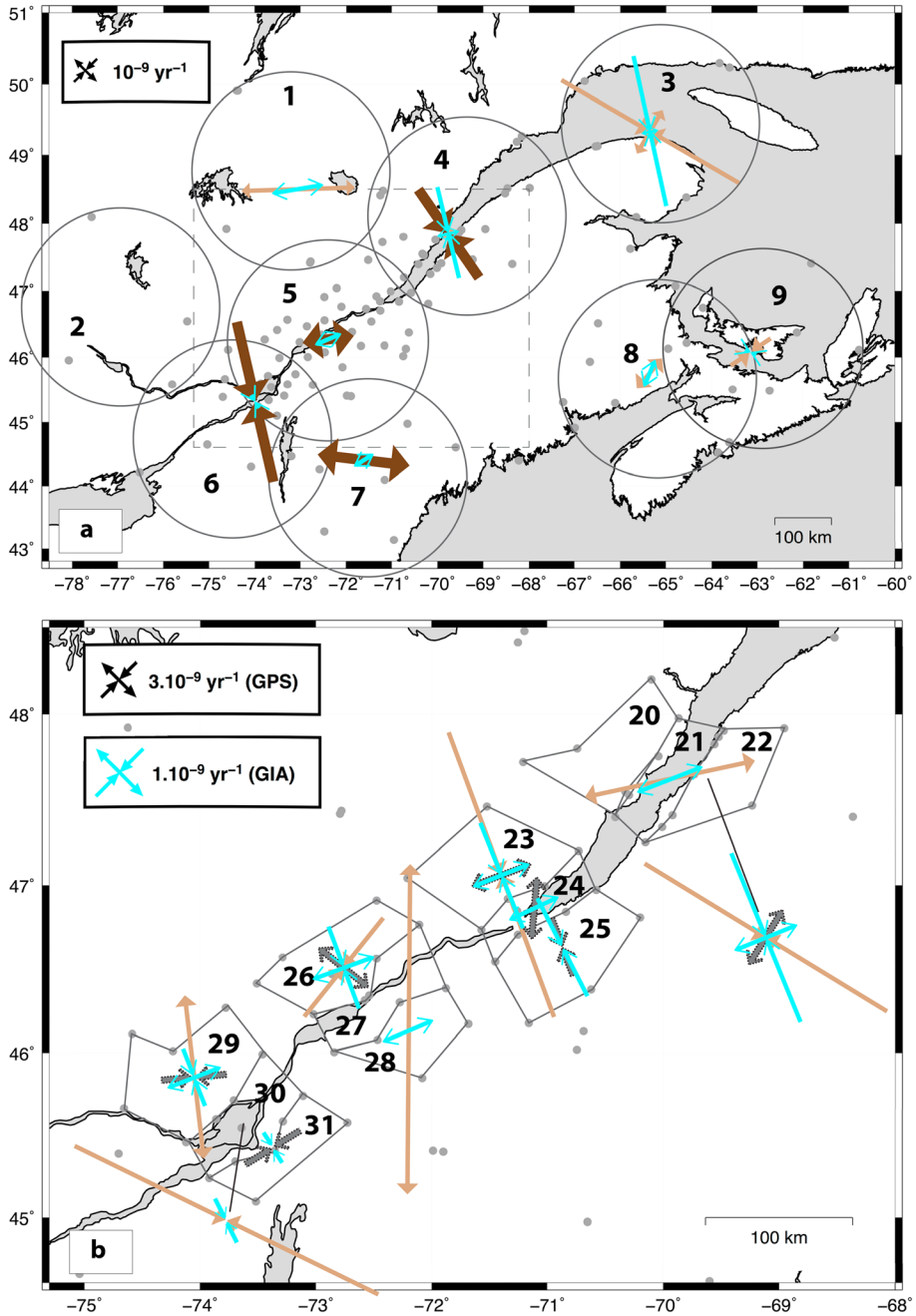

Figure 9. Horizontal Global Positioning System (GPS) and glacial isostatic adjustment (GIA) model strain rates. Dark brown, light brown, and gray arrows show GPS strain rates of categories A–C. Light blue arrows show GIA strain rates based on ICE6G_C (VM5a) model (Peltier et al., 2015) interpolated at the GPS sites. (a) and (b) show the large and short spatial scales, respectively (cf. Figures 8a and 8c). Note the difference of scale between GPS and GIA strain rates in (b). The dashed rectangle in a shows delimitation of the map in (b).

At the smaller spatial scales (Figure 9b), GPS and GIA model strain rates show consistent deformation style (except zones 26, 29, and 31) confirming GIA as being the primary deformation process measured by GPS, even at low spatial scale (50–100 km). However, strong differences in magnitude between GPS and GIA model strain rates are observed. On average, GPS strain rates in the structural inheritance area are 14 times larger than those from the GIA model, with a GPS/GIA strain rate ratio spanning 6 to 28. Considering the standard error of GPS strain rate the GPS/GIA strain rate ratios are on average from 2 to 25 (ratios and respective

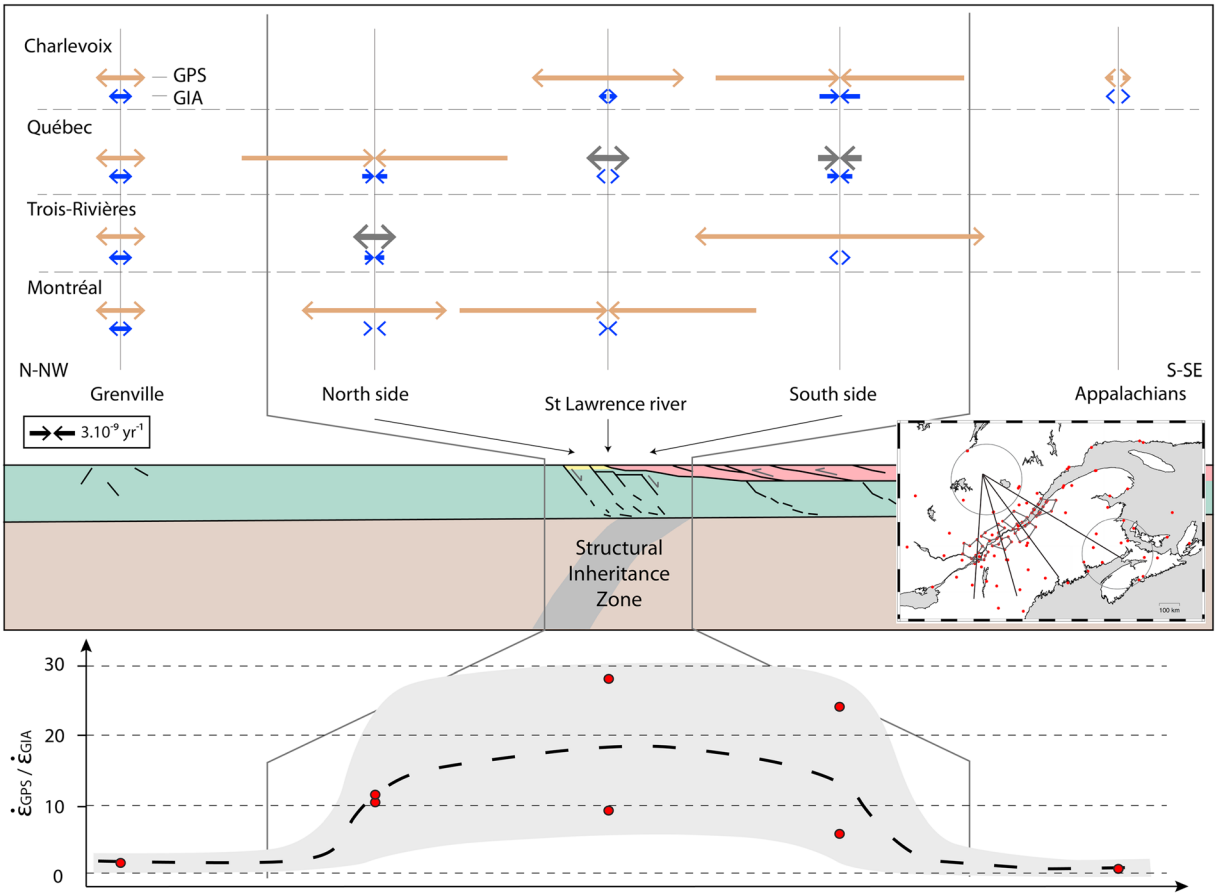

Figure 10. (top) Schematic profiles of strain rate variations in eastern Canada and the Saint Lawrence Valley. Light brown and gray vectors show Global Positioning System (GPS) strain rates with a robustness categories of B and C, respectively; blue vectors show glacial isostatic adjustment (GIA) model strain rates. The Grenville and Appalachians provinces are represented by a unique strain rate (zones 1 and 8; see map bottom right corner). Zones 21 and 22; 23–25; 26 and 28; and 29 and 30 are used in the Charlevoix, Québec, Trois-Rivières, and Montréal profile, respectively (see Figure 9). (bottom) Average variations of the GPS/GIA strain rate ratio (i.e., strain rate amplification). Red points show calculated strain rate ratios for each zone (supporting information Table S5). The dashed line and gray shading represent the mean and 67% confidence interval of these ratios.

uncertainty are provided in Table S5 in the supporting information). Thus, in the structural inheritance area, the GPS strain rates are significantly higher than the GIA strain rates.

One limitation of this comparison is the variability of GIA models that leads to different velocity fields, which can change the associated strain rates (e.g., Sella et al., 2007). A comparison of the strain rates predicted by the most recent ICE6G_C and older ICE5G models (with two different mantle viscosity structure VM2 and VM4) is presented in Figure S4 in the supporting information. The magnitude of the GIA strain rates is maintained between the various models, confirming our comparative GPS-GIA analysis. The NE-SW extension is preserved between the three GIA models. The only significant difference is that the ICE6G_C model predicts NW-SE shortening whereas no detectable deformation on that component is predicted by the ICE5G_VM4 model and NW-SE extension is predicted by the ICE5G_VM2 model.

5. Discussion

Figure 10 summarizes the main results through schematic strain rate profiles across the Saint Lawrence Valley in four zones: Charlevoix, Québec City, Trois-Rivières, and Montréal. Profiles are roughly oriented NW-SE or NNW-SSE, from the Grenville to Appalachians provinces. The Grenville province is associated with a single region in the strain rate analysis (Figure 8a), which is displayed on the four profiles. The Appalachians province is also associated with a single region and is used for the Charlevoix profile. This figure highlights the role of structural inheritance on the localization of present-day deformation. GPS deformation styles

generally correspond to the GIA deformation styles (except on the north side of Montréal and Trois-Rivières), indicating that the GPS signal is mainly caused by GIA process. Additionally, the GPS signal is amplified within the area of structural inheritance (the Saint Lawrence Valley). On average the GPS strain rates in the structural inheritance area are 14 times higher than those from the GIA model, with a GPS/GIA strain rate ratio spanning 6 to 28 (cf. Table S5 in the supporting information).

This is the first quantification of surface strain amplification due to structural inheritance. This strain amplification could be due to a weakened rheology of the paleostructures (e.g., Mazzotti & Gueydan, 2017). The impact of a weakened rheology on surface strain was previously proposed on the basis of numerical modeling. Grollimund and Zoback (2001) proposed that a local weak zone in the lithospheric mantle, with a reduction of effective viscosity of one order of magnitude compared to the surrounding, result in GIA strain rate increase by 2 to 3 orders of magnitude in the New Madrid area, central United States. The effect of a weak zone was also investigated in southeastern Canada by Wu and Mazzotti (2007). Their reference GIA model (without a weak zone) displays surface strain rates of (1.0–1.5) $\times 10^{-9}$ year^{-1}, similar to those observed in the Greenville and Appalachians provinces (Figures 8a and 9a). With a lithospheric vertical weak zone associated with the Iapetan structures of the Saint Lawrence Valley, the predicted GIA strain rates reach (4–5) $\times 10^{-9}$ year^{-1}, implying a structural inheritance impact of a factor of 3–4, lower than the range of factor of 6 to 28 that we found between GPS and GIA model strain rates (Figures 9b and 10).

Under the hypothesis of structural inheritance producing significant strain concentration, the entire Saint Lawrence Valley should display similar deformation patterns to first order. Yet we observe strong spatial variations of GPS strain rates (Figures 8c and 10) and seismicity (Figure 3) within the structural inheritance area. The strong lateral variations of deformation style along the Saint Lawrence Valley are explained by the GIA process in most areas (except in zones 26, 29 and 31; Figures 9b and 10).

GPS strain rates found in the Saint Lawrence and Appalachians provinces are on average 15×10^{-9} and 1×10^{-9} year^{-1}, respectively (Table 2), whereas seismic strain rates for same areas are on average 0.7×10^{-9} and 0.01×10^{-9} year^{-1} (Mazzotti & Adams, 2005), respectively, 20 and 100 times smaller. This first-order comparison suggests that most of the GPS signal corresponds to aseismic (likely elastic) deformation driven by GIA, with only a small fraction (1–5%) of this ongoing deformation expressed in the present-day seismicity. Additional complexities for this comparison between GPS and seismic signals exist since intraplate active seismic areas might migrate in time (Liu et al., 2011; Stein et al., 2009).

6. Conclusions

The role of structural inheritance, defined as lithospheric-scale paleotectonic structures (Figure 2), is a major element in the understanding of intraplate deformation and earthquake dynamics. The Saint Lawrence Valley is a key area to investigate this role, with GPS stations outside and inside the structural inheritance area (Figure 4). The analysis of these GPS data yield three main observations:

1. Structural inheritance leads to significant concentration of the present-day deformation, with GPS strain rates higher by a factor of 2–11 in the Saint Lawrence Valley compared to Grenville and Appalachians provinces (Figures 8a and 10).
2. GPS and GIA strain rates display same deformation style (except zones 26, 29, and 31), suggesting that the GIA process is at the origin of the GPS signal.
3. Compared to GIA model, GPS strain rates are 14 times higher on average in the Saint Lawrence Valley, which we interpret as the effect of GIA strain concentration in a region of weakened rheology due to the structural inheritance (cf. Wu & Mazzotti, 2007). Outside of the structural inheritance area, GPS strain rates are on average 1–3 times higher than GIA strain rates (Figures 9b and 10).

We observe no systematic correlation between seismicity and GPS strain rate patterns, both witnesses of present-day deformation. Our first-order results suggest that the GPS deformation is mostly elastic (up to 99%). This hypothesis can be tested with numerical modeling of recent (postdeglaciation) deformation, including tectonic inheritance weakening and local rheology variations. The integration of continuous and campaign GPS data is a key element to calculate strain rates at different spatial scale. Continuing the campaign surveys should allow clarifying the spatially heterogeneous strain rates within the structural inheritance area.

Acknowledgments

We thank J. Weber and anonymous reviewers for their very constructive suggestions that strongly improved the paper. We thank all the colleagues and students who contributed to the numerous Saint Lawrence GPS campaigns since 2005, in particular Rock Santerre, Stéphanie Bourgon, and Marc Cocard from Université Laval, Québec, and the field survey teams of NRCan Geodetic Survey and Geological Survey of Canada. We thank the Ministère des Ressources naturelles et de la Faune of Quebec for making available the data for their continuous GPS network. Data for the CACS and United States continuous GPS networks are available through NRCan and NGS (CORS) archives. Data for the campaign networks are available by request to the authors. This work was supported by the Natural Resources Canada's Public Safety Geoscience Program, the Canadian Geodetic Survey, and by the French Agence National de la Recherche through grant ANR-12-CHEX-0004-01 to S. M.

References

Adams, J., & Basham, P. W. (1991). The seismicity and seismotectonics of eastern Canada. In D. B. Slemmons, et al. (Eds.), *Neotectonics of North America, decade map* (Vol. 1, pp. 261–276). Colorado: Geological Society of America Boulder.

Altamimi, Z., Métivier, L., & Collilieux, X. (2012). ITRF2008 plate motion model. *Journal of Geophysical Research*, *117*, B07402. https://doi.org/10.1029/2011JB008930

Baird, A. F., McKinnon, S. D., & Godin, L. (2009). Stress channelling and partitioning of seismicity in the Charlevoix seismic zone, Québec, Canada. *Geophysical Journal International*, *179*(1), 559–568. https://doi.org/10.1111/j.1365-246X.2009.04275.x

Boehm, J., Werl, B., & Schuh, H. (2006). Troposphere mapping functions for GPS and very long baseline interferometry from European Centre for Medium-Range Weather Forecasts operational analysis data. *Journal of Geophysical Research*, *111*, B02406. https://doi.org/10.1029/2005JB003629

Calais, E., Mattioli, G., DeMets, C., Nocquet, J.-M., Stein, S., Newman, A., & Rydelek, P. (2005). Seismology: Tectonic strain in plate interiors? *Nature*, *438*(7070), E9–E10. https://doi.org/10.1038/nature04428

Coppersmith, K. J., Johnston, A. C., Metzger, A. G., & Arabasz, W. J. (1987). Methods for assessing maximum earthquakes in the central and eastern United States, Electric Power Research Institute, working report EPRI RP2556-12 (pp. 312).

Craig, T. J., & Calais, E. (2014). Strain accumulation in the New Madrid and Wabash Valley seismic zones from 14 years of continuous GPS observation. *Journal of Geophysical Research: Solid Earth*, *119*, 9110–9129. https://doi.org/10.1002/2014JB011498

Dow, J. M., Neilan, R. E., & Rizos, C. (2009). The International GNSS Service in a changing landscape of Global Navigation Satellite Systems. *Journal of Geodesy*, *83*(3–4), 191–198. https://doi.org/10.1007/s00190-008-0300-3

Dyke, A. S. (2004). An outline of North American Deglaciation with emphasis on central and northern Canada. In J. Ehlers & P. L. Gibbard (Eds.), *Quaternary glaciations: Extent and chronology, part II* (Vol. 2b, pp. 373–424). Amsterdam: Elsevier.

El-Fiky, G. S., Kato, T., & Fujii, Y. (1997). Distribution of vertical crustal movement rates in the Tohoku district, Japan, predicted by least-squares collocation. *Journal of Geodesy*, *71*(7), 432–442. https://doi.org/10.1007/s001900050111

Frankel, A., Smalley, R., & Paul, J. (2012). Significant motions between GPS sites in the New Madrid region: Implications for seismic hazard. *Bulletin of the Seismological Society of America*, *102*(2), 479–489. https://doi.org/10.1785/0120100219

Gordon, R. G. (1998). The plate tectonic approximation: Plate nonrigidity, diffuse plate boundaries, and global plate reconstructions. *Annual Review of Earth and Planetary Sciences*, *26*(1), 615–642. https://doi.org/10.1146/annurev.earth.26.1.615

Goudarzi, M. A., Cocard, M., & Santerre, R. (2015). GeoStrain: An open source software for calculating crustal strain rates. *Computers & Geosciences*, *82*, 1–12. https://doi.org/10.1016/j.cageo.2015.05.007

Goudarzi, M. A., Cocard, M., & Santerre, R. (2016). Present-day 3D velocity field of eastern North America based on continuous GPS observations. *Pure and Applied Geophysics*, *173*(7), 2387–2412. https://doi.org/10.1007/s00024-016-1270-7

Grollimund, B., & Zoback, M. D. (2001). Did deglaciation trigger intraplate seismicity in the New Madrid seismic zone? *Geology*, *29*(2), 175–178 . https://doi.org/10.1130/0091-7613(2001)029<0175:DDTISI>2.0.CO;2

Gueydan, F., Morency, C., & Brun, J.-P. (2008). Continental rifting as a function of lithosphere mantle strength. *Tectonophysics*, *460*(1-4), 83–93. https://doi.org/10.1016/j.tecto.2008.08.012

Hackl, M., Malservisi, R., Hugentobler, U., & Wonnacott, R. (2011). Estimation of velocity uncertainties from GPS time series: Examples from the analysis of the South African TrigNet network. *Journal of Geophysical Research*, *116*, B11404. https://doi.org/10.1029/2010JB008142

Hackl, M., Malservisi, R., & Wdowinski, S. (2009). Strain rate patterns from dense GPS networks. *Natural Hazards and Earth System Sciences*, *9*(4), 1177–1187. https://doi.org/10.5194/nhess-9-1177-2009

Henton, J. A., Craymer, M. R., Ferland, R., Dragert, H., Mazzotti, S., & Forbes, D. L. (2006). Crustal motion and deformation monitoring of the Canadian landmass. *Geomatica*, *60*, 173–191.

Héroux, P., & Kouba, J. (2001). GPS Precise Point Positioning using IGS orbit products. *Physics and Chemistry of the Earth*, *26*(6–8), 573–578. https://doi.org/10.1016/S1464-1895(01)00103-X

Herring, T. A., King, R. W., Floyd, M. A., & McClusky, S. C. (2015). *Introduction to GAMIT/GLOBK, release 10.6*. Cambridge: Massachusetts Institute of Technologie.

Hoffman, F. P. (1991). Did breakout of Laurentia turn Gondwana inside-out? *Science*, *252*(5011), 1409–1412. https://doi.org/10.1126/science.252.5011.1409

Johnston, A. C. (1989). The seismicity of "stable continental interiors". In S. Gregersen & P. W. Basham (Eds.), *Earthquakes at North-Atlantic passive margins: Neotectonics and postglacial rebound* (pp. 299–327). Dordrecht, Netherlands: Kluwer Academic Publishers.

Karlstrom, K. E., Åhäll, K. I., Harlan, S. S., Williams, M. L., McLelland, J., & Geissman, J. W. (2001). Long-lived (1.8–1.0 Ga) convergent orogen in southern Laurentia, its extensions to Australia and Baltica, and implications for refining Rodinia. *Precambrian Research*, *111*(1-4), 5–30. https://doi.org/10.1016/S0301-9268(01)00154-1

Kumarapeli, P. S. (1985). Vestiges of Iapetan rifting in the craton west of the northern Appalachians. *Geoscience Canada*, *12*, 54–59.

Kumarapeli, P. S., & Saull, V. A. (1966). The St. Lawrence Valley system: A north American equivalent of the East African Rift Valley system. *Canadian Journal of Earth Sciences*, *3*(5), 639–658. https://doi.org/10.1139/e66-045

Lamontagne, M., Keating, P., & Toutin, T. (2000). Complex faulting confounds earthquake research in the Charlevoix seismic zone, Québec. *Eos*, *81*(26), 289–293. https://doi.org/10.1029/00EO00213

Lamontagne, M., & Ranalli, G. (2014). Earthquakes and geological structures of the St. Lawrence Rift System. In P. Talwani (Ed.), *Intraplate earthquakes* (pp. 72–97). Cambridge: Cambridge University Press.

Lamothe, P., Santerre, R., Cocard, M., & Mazzotti, S. (2010). A crustal deformation study of the Charlevoix Seismic Zone in Quebec. *Geomatica*, *64*(3), 61–71.

Langbein, J. (2008). Noise in GPS displacement measurements from Southern California and Southern Nevada. *Journal of Geophysical Research*, *113*, B05405. https://doi.org/10.1029/2007JB005247

Lemieux, Y., Tremblay, A., & Lavoie, D. (2003). Structural analysis of supracrustal faults in the Charlevoix area, Québec: Relations to impact cratering and the St-Laurent fault system. *Canadian Journal of Earth Sciences*, *40*(2), 221–235. https://doi.org/10.1139/e02-046

Liu, M., Stein, S., & Wang, H. (2011). 2000 years of migrating earthquakes in North China: How earthquakes in midcontinents differ from those at plate boundaries. *Lithosphere*, *3*(2), 128–132. https://doi.org/10.1130/L129.1

Lyard, F., Lefevre, F., Letellier, T., & Francis, O. (2006). Modelling the global ocean tides: Modern insights from FES2004. *Ocean Dynamics*, *56*(5–6), 394–415. https://doi.org/10.1007/s10236-006-0086-x

Malservisi, R., Hugentobler, U., Wonnacott, R., & Hackl, M. (2013). How rigid is a plate? Geodetic constraint from the TrigNet CGPS network, South Africa. *Geophysical Journal International*, *192*(3), 918–928. https://doi.org/10.1093/gji/ggs081

Malvern, L. E. (1969). *Introduction to the mechanics of a continuous media, 713*. Upper Saddle River, NJ: Prentice-Hall.

Mao, A., Harrison, C. G. A., & Dixon, T. H. (1999). Noise in GPS coordinate time series. *Journal of Geophysical Research*, *104*(B2), 2797–2816. https://doi.org/10.1029/1998JB900033

Marechal, A., Mazzotti, S., Elliott, J. L., Freymueller, J. T., & Schmidt, M. (2015). Indentor-corner tectonics in the Yakutat-St. Elias collision constrained by GPS. *Journal of Geophysical Research: Solid Earth*, *120*, 3897–3908. https://doi.org/10.1002/2014JB011842

Mazzotti, S. (2007). Geodynamic models for earthquake studies in intraplate North America. In S. Stein & S. Mazzotti (Eds.), *Continental intraplate earthquakes: Science, hazard and policy issues* (Vol. 425, pp. 17–33). Boulder, CO: Geological Society of America Special Paper. https://doi.org/10.1130/2007.2425(02)

Mazzotti, S., & Adams, J. (2005). Rates and uncertainties on seismic moment and deformation in eastern Canada. *Journal of Geophysical Research*, *110*, B09301. https://doi.org/10.1029/2004JB003510

Mazzotti, S., & Gueydan, F. (2017). Control of tectonic inheritance on continental intraplate strain rate and seismicity. *Tectonophysics*. https://doi.org/10.1016/j.tecto.2017.12.014

Mazzotti, S., James, T. S., Henton, J., & Adams, J. (2005). GPS crustal strain, postglacial rebound, and seismic hazard in eastern North America: The Saint Lawrence valley example. *Journal of Geophysical Research*, *110*, B11301. https://doi.org/10.1029/2004JB003590

Mazzotti, S., & Townend, J. (2010). State of stress in central and eastern North American seismic zones. *Lithosphere*, *2*(2), 76–83. https://doi.org/10.1130/L65.1

Musacchio, G., Mooney, W. D., Luetgert, J. H., & Christensen, N. I. (1997). Composition of the crust in the Grenville and Appalachian Provinces of North America inferred from *Vp/Vs* ratios. *Journal of Geophysical Research*, *102*(B7), 15,225–15,241. https://doi.org/10.1029/96JB03737

Nguyen, H. N., Vernant, P., Mazzotti, S., Khazaradze, G., & Asensio, E. (2016). 3D GPS velocity field and its implications on the present-day post-orogenic deformation of the Western Alps and Pyrenees. *Journal of Geophysical Research: Solid Earth*, *7*, 1349–1363. https://doi.org/10.5194/se-2016-78

Njoroge, M., Malservisi, R., Voytenko, D., & Hackl, M. (2015). Is Nubia Plate Rigid? A Geodetic Study of the Relative Motion of Different Cratonic Areas Within Africa. In T. van Dam (Eds), *REFAG 2014, International Association of Geodesy Symposia* (Vol. 146, pp. 171–180). https://doi.org/10.1007/1345_2015_212

Parent, M., & Occhietti, S. (1988). Late Wisconsinan deglaciation and Champlain Sea invasion in the St. Lawrence Valley, Québec. *Géographie Physique et Quaternaire*, *42*(3), 215–246. https://doi.org/10.7202/032734ar

Peltier, W. R., Argus, D. F., & Drummond, R. (2015). Space geodesy constrains ice-age terminal deglaciation: The global ICE-6G_C (VM5a) model. *Journal of Geophysical Research: Solid Earth*, *120*, 450–487. https://doi.org/10.1002/2014JB011176

Rankin, D. W. (1975). The continental margin of eastern North America in the southern Appalachians: The opening and closing of the Proto-Atlantic Ocean. *American Journal of Science*, *275A*, 298–336.

Rondot, J. (1968). Nouvel impact meteoritique fossile? La structure semi-circulaire de Charlevoix. *Canadian Journal of Earth Sciences*, *5*(5), 1305–1317. https://doi.org/10.1139/e68-128

Santamaría-Gómez, A., Bouin, M.-N., Collilieux, X., & Wöppelmann, G. (2011). Correlated errors in GPS position time series: Implications for velocity estimates. *Journal of Geophysical Research*, *116*, B01405. https://doi.org/10.1029/2010JB007701

Sella, G. F., Stein, S., Dixon, T. H., Craymer, M., James, T. S., Mazzotti, S., & Dokka, R. K. (2007). Observation of glacial isostatic adjustment in "stable" North America with GPS. *Geophysical Research Letters*, *34*, L02306. https://doi.org/10.1029/2006GL027081

Stein, S., Liu, M., Calais, E., & Li, Q. (2009). Mid-continent earthquakes as a complex system. *Seismological Research Letters*, *80*(4), 551–553. https://doi.org/10.1785/gssrl.80.4.551

Stein, S., & Mazzotti, S. (2007). *Continental intraplate earthquakes: Science, hazard, and policy issues*. Boulder, CO: The Geological Society of America Special Paper 425.

Thomas, W. A. (2006). Tectonic inheritance at a continental margin. *GSA Today*, *16*(2), 4–11. https://doi.org/10.1130/1052-5173(2006)016[4:TIAACM]2.0.CO;2

Tremblay, A., Long, B., & Massé, M. (2003). Supracrustal faults of the St. Lawrence rift system, Quebec: Kinematics and geometry as revealed by field mapping and marine seismic reflection data. *Tectonophysics*, *369*(3-4), 231–252. https://doi.org/10.1016/S0040-1951(03)00227-0

Tushingham, A. M., & Peltier, W. R. (1991). Ice–3G: A new global model of late Pleistocene deglaciation based upon geophysical predictions of post-glacial relative sea level change. *Journal of Geophysical Research*, *96*(B3), 4497–4523. https://doi.org/10.1029/90JB01583

Wdowinski, S., Bock, Y., Zhang, J., Fang, P., & Genrich, J. (1997). Southern California Permanent GPS Geodetic Array: Spatial filtering of daily positions for estimating coseismic and postseismic displacements induced by the 1992 Landers earthquake. *Journal of Geophysical Research*, *102*, 4497–4523. https://doi.org/10.1029/90JB01583

Williams, S. D. P. (2003). The effect of coloured noise on the uncertainties of rates estimated from geodetic time series. *Journal of Geodesy*, *76*(9–10), 483–494. https://doi.org/10.1007/s00190-002-0283-4

Williams, S. D. P., Bock, Y., Fang, P., Jamason, P., Nikolaidis, R. M., Prawirodirdjo, L., et al. (2004). Error analysis of continuous GPS position time series. *Journal of Geophysical Research*, *109*, B03412. https://doi.org/10.1029/2003JB002741

Wu, P., & Johnston, P. (2000). Can deglication trigger earthquakes in N. America? *Geophysical Research Letters*, *27*(9), 1323–1326. https://doi.org/10.1029/1999GL011070

Wu, P., & Mazzotti, S. (2007). Effects of a lithospheric weak zone on postglacial seismotectonics in eastern Canada and northeastern USA. In S. Stein & S. Mazzotti (Eds.), *Continental intraplate earthquakes: Science, hazard and policy issues* (Vol. 425, pp. 285–298). Boulder, CO: Geological Society of America Special Paper. https://doi.org/10.1130/2007.2425(09)

Zhu, Z., Zhou, X., Deng, L., Wang, K., & Zhou, B. (2017). Quantitative analysis of geophysical sources of common mode component in CMONOC GPS coordinate time series. *Advances in Space Research*, *60*(12), 2896–2909. https://doi.org/10.1016/j.asr.2017.05.002